

RSC Advances



This is an *Accepted Manuscript*, which has been through the Royal Society of Chemistry peer review process and has been accepted for publication.

Accepted Manuscripts are published online shortly after acceptance, before technical editing, formatting and proof reading. Using this free service, authors can make their results available to the community, in citable form, before we publish the edited article. This *Accepted Manuscript* will be replaced by the edited, formatted and paginated article as soon as this is available.

You can find more information about *Accepted Manuscripts* in the [Information for Authors](#).

Please note that technical editing may introduce minor changes to the text and/or graphics, which may alter content. The journal's standard [Terms & Conditions](#) and the [Ethical guidelines](#) still apply. In no event shall the Royal Society of Chemistry be held responsible for any errors or omissions in this *Accepted Manuscript* or any consequences arising from the use of any information it contains.



RSC ADVANCES

ARTICLE

Modelling of Cracks Developed in Lithium-ion Cells under Mechanical Loading

Elham Sahraei,^a Michael Kahn,^b Joseph Meier,^c and Tomasz Wierzbicki^a

Received 00th January 20xx,
Accepted 00th January 20xx

DOI: 10.1039/x0xx00000x

www.rsc.org/

This research reports on an experimental and numerical study of material failure in the electrode assemblies (i.e. “jelly roll” and/or “electrode stack”) of lithium-ion batteries after local mechanical loading. Deformed cylindrical and pouch cells (i.e. lithium-ion polymer cells) were subjected to X-ray computed tomography (CT scanning) to detect location, size, and orientation of cracks that developed in the electrode assemblies at onset of short-circuit. An experimental program was completed to acquire properties of electrode-separator micro components of electrode assemblies in tension. This data was used for calibration of an anisotropic material model. Finite element models were developed for both cell types and a maximum strain criteria was used for element failure and deletion at short circuit. The models developed here predict location of cracks in both pouch and cylindrical cells. The finite element models corroborated the CT scan regarding location and orientation of cracks formed in the electrode assemblies. In both pouch and cylindrical cells, cracks were found to initiate perpendicular to the transverse direction of the separator.

Introduction

Use of lithium-ion batteries in electric vehicles brings with itself the need to understand the outcome of mechanical damage to battery packs or cells; regardless of the amount of protection around the battery pack, it is impossible to assure zero deformation of the battery cells at high accelerations during a severe vehicle crash. Currently, the mechanical deformation of batteries is not a major issue for stationary uses, but this is not the case for automobile applications. As manufacturers continue to increase the energy stored in cells, mechanical deformation and cell failure is an increasingly important issue. There is much less research available in the area of mechanical failure compared to the research available addressing thermal and electrochemical failure modes. Recent studies have reported on mechanical tests and finite element modelling of pouch and cylindrical cells or components^{1–8}. Some studies have shown possible methods of predicting failure and onset of short circuit under mechanical deformation^{1,3,4,6}. The first generation of isotropic finite element models developed by the present team was able to accurately predict the load-displacement curves during a local indentation for both pouch and cylindrical batteries. The model also provided a precise prediction of load and

deformation under which an internal short circuit was initiated in the cell. An internal short circuit is a condition that may lead to thermal runaway of lithium-ion batteries in some cases. Upon separator failure, four types of negative-positive electrode contacts are possible within the electrode assembly. Internal short circuits may occur by contact between (a) the positive and negative active materials, (b) positive active material and negative current collector, (c) negative active material and positive current collector, and/or (d) positive and negative current collectors. Each type of contact has a different heating characteristic⁹. Thus, internal short circuits are a challenging phenomenon from an electrochemical and thermal modelling standpoint. Further advancements are still needed to predict the probability of lithium-ion battery thermal runaway occurring after an internal short circuit.

Experiments and models involving thermal/electrochemical behaviour of cells during normal operation or after induced electric short circuits have been studied^{10–12}. In order to couple the existing thermal/electrochemical data with the mechanical model of the cell, it is necessary to determine:

- i) Location of mechanical failure within the electrode assembly
- ii) Crack orientation
- iii) Size of the fractured region

To understand the above parameters, selected cells tested up to onset of short circuit were sent to Exponent for X-ray computed tomography (CT scanning). CT scanning has been used in literature for in-situ investigations of batteries and their failure^{13,14}. However, not used for detection of crack formation due to mechanical failure in the cell. Images and 3D reconstructions from CT scanning revealed the location, shape, and size of interior failure of the electrode assemblies, which

^a Impact and Crashworthiness Lab, Department of Mechanical Engineering, MIT.

^b Exponent Inc., Menlo Park, CA.

^c US Navy, Moosup, Connecticut.

† Footnotes relating to the title and/or authors should appear here.

Electronic Supplementary Information (ESI) available: [details of any supplementary information available should be included here]. See DOI: 10.1039/x0xx00000x

was not evident from inspection of the exterior of the cylindrical cell can or soft aluminium cell pouch. An experimental program was developed and tensile properties of micro components of electrode assemblies were measured and documented. It was observed that the separator has two distinct axes of anisotropy: in the Machine (roll) Direction (MD) of the separator and in the Transverse Direction (TD).

The anisotropic properties of electrode assembly components - especially the separator, motivated development of anisotropic models of the electrode assembly. The anisotropic model provided a close prediction of the geometry of deformation and size and shape of cracks formed inside electrode assembly under mechanical loading.

CT-Scan of Mechanically Deformed Cells

Two types of cells were used for this study, a small pouch cell and an 18650 cylindrical cell. The cells were new (not cycled) and were discharged to an SOC of less than 10% before testing. By disc arching the cells, it was ensured that cells will not go through a thermal runaway, and location of failure will not get distorted due to thermal damage and can be investigated through CT-Scanning. During the tests, the cells were resting on a rigid platform and deformed by rigid metallic punches which indented the cells at a constant speed of 1 mm/min. Force, displacement, temperature, and voltage of the cells were monitored during the testing. The force applied increased with an increase in the depth of deformation, while the temperature and voltage remained constant. After few millimetres of deformation, a drop in force simultaneous with a drop in voltage and a rise in temperature indicated that a short circuit occurred in the cell. The benefit of discharging the cells before testing was that the short circuit did not cause any extreme thermal events which otherwise could have potentially damaged the electrode assembly and inhibited detection of the exact location of failure at onset of short circuit. Visual inspection of exterior pouch and can of the cells did not show any failure of exterior covers during these tests. The tested cells were subjected to X-ray computed tomography (CT scanning) to detect the extent of damage to electrode assembly without invasive destruction of the cells. Characteristics and size of the two cells tested are reported in Table 1.

Table 1: Specifications of small pouch cells and 18650 cylindrical cells used for this research

	Small Pouch Cell	18650 Cylindrical Cell
Chemistry	LiCoO ₂ /graphite	LiCoO ₂ /graphite
Nominal Capacity	740 mAh	2400 mAh
Nominal Voltage	3.7 V	3.7 V
Thickness/ Diameter	5.35 mm	18 mm
Width	34 mm	
Length	59.5 mm	65 mm
Weight	19 g	47.0 g

X-ray computed tomography (CT scanning) is a powerful non-destructive examination technique that has applications in a variety of industrial and medical applications. CT scanning is frequently used as a tool for failure analysis, and is particularly useful for examining objects poorly suited to be disassembled, such as batteries. For the present work, CT scanning was carried out at Exponent, Inc. of Menlo Park, CA on a Varian Medical Systems Desktop Cabinet Unit, part number 8020-0001 (Varian Medical Systems, Lincolnshire, IL). In CT scanned images, a higher intensity (i.e. brighter) pixels indicate material of higher X-ray absorbance. For example, a steel case of an 18650 cell appears brighter than a soft aluminium foil pouch of a lithium-ion polymer cell due to the higher density of iron compared to aluminium. Further details about the CT scan method are included in Appendix 1.

Figure 1a) depicts a longitudinal cross-section through the crimp region of the subject 18650 battery cell from the present work, and illustrates materials of various densities found within the cell. Figure 1b) shows an example of cropping into a 3D rendering of the subject 18650 battery cell from the present work. Figure 1c) shows CT cross-sections taken at two different locations: the upper pair of images depicts the first location near the top of the 18650 electrode assembly, while the bottom pair of images depicts a second location at the center of the indentation. Left images depict longitudinal cross-sections, and right images depict axial cross-sections. Thus, complex geometrical features such as cracks within electrode assemblies of sealed battery cells can be imaged, virtually cross-sectioned, and their features can be measured. CT image processing as described here was performed using OsiriX 64-bit software.

Isotropic Material Model with Element Erosion

A computational model developed by the present authors gives good results in predicting the strength and deformation of the cell as well as the maximum tolerated load and displacement at onset of short circuit^{1,3,4}. The homogenized isotropic model of the cell assumes a plastic potential function in the space of principal stresses.

$$f_i = |\sigma_i| - Y \quad (1)$$

where the yield stress is defined differently in compression and tension by

$$\begin{aligned} Y &= Y_c + H(\epsilon_v) \quad \text{for } \sigma_i < 0 (\text{compression}) \\ Y &= Y_t \quad \text{for } \sigma_i > 0 (\text{tension}) \end{aligned} \quad (2)$$

in which Y_t is a constant tension cut off value, the initial yield in compression (Y_c) is almost zero, and the volumetric hardening $H(\epsilon_v)$ is assumed to be described by a power function:

$$\sigma = A\varepsilon^n \quad (3)$$

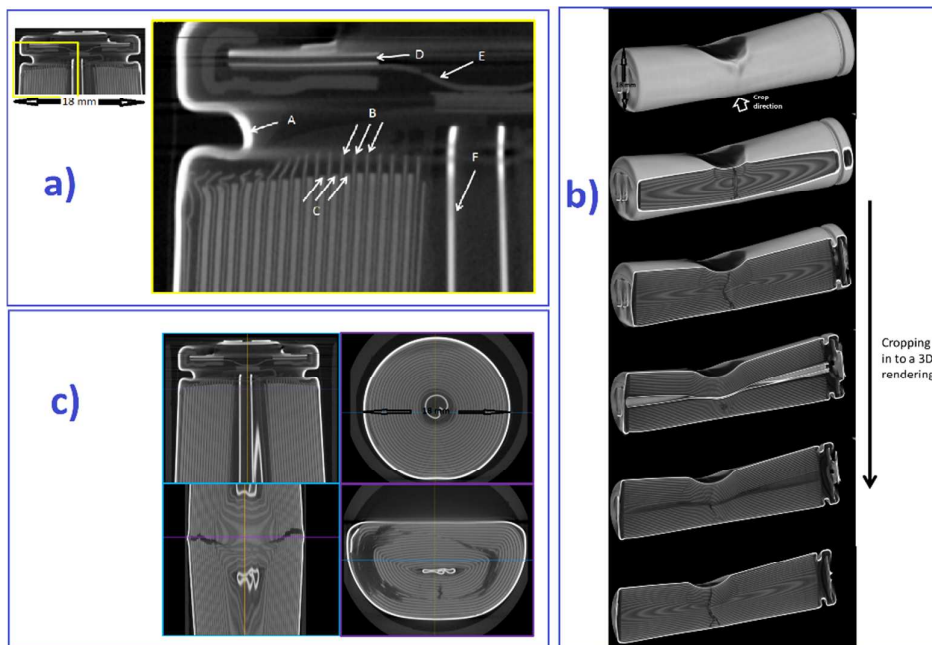


Figure 1: a) Longitudinal cross-section through 18650 crimp region: (A) steel cell can, (B) edges of negative electrode, (C) edges of positive electrode, (D) positive temperature coefficient (PTC) device, (E) aluminium safety vent, (F) steel center pin, b) A series of images depicting cropping into a 3D rendering of the subject 18650 from the present work, c) CT cross-sections of the 18650 cylindrical cell

Element erosion was used to visualize the formation of cracks. An element is taken to be deleted when the maximum principal tensile strain reaches its critical value (ε_f). The value of ε_f was obtained by reverse engineering method using the cell level test.

Strengths and Limitations of the isotropic Representative Volume Element (RVE) in Predicting Crack.

Considered in this section are cell models for a small pouch cell and an 18650 cylindrical cell. The cell models were created from measured dimensions and observed geometry using Altair Hypermesh. Pouch elements were 1x1x0.48 mm, and cylindrical cell elements were 0.8x0.8x0.8 mm. LS Dyna nonlinear finite element software was used for modelling. In this modelling approach, all the components of the electrode/separator assembly is lumped into a representative volume element which has cumulative effects of mechanical properties of all layers in the assembly. For further information about the cells and details of the tests and isotropic modelling approach, please see two earlier publications by Sahraei et al, 2012^{1,3}. In this research, element erosion feature was added to the original models to track down the progression of the fracture process inside the cells. The maximum principal tensile strain failure criteria was used to trigger element erosion.

Pouch Cell: The revised isotropic model with element erosion feature had good predictability in terms of load-displacement and detecting onset of internal short circuit in hemispherical

punch loading. However, the focus of this research was to evaluate the location of cracks as observed in the finite element simulation versus a CT scan of the cell. As shown in Figure 2, the failure observed in the isotropic model of the pouch was in a round area right under the pouch, while, the CT scan shows a linear crack perpendicular to the TD of the separator. Therefore, this model was not capable of predicting the crack correctly for this type of cell.

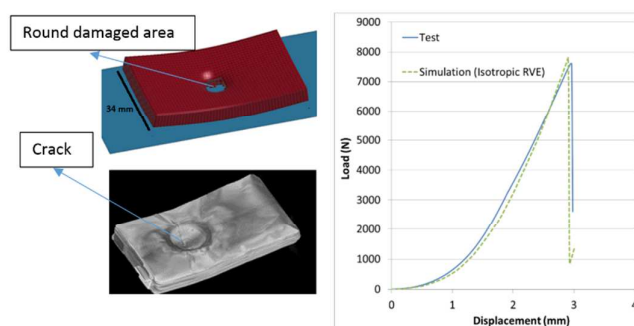


Figure 2: Location of failure in isotropic model of small pouch versus CT-Scan.

Cylindrical Cell: The next case was the model of an 18650 cylindrical cell. In the original model of an 18650 cell, all cell internal components within the casing were lumped into homogenized solid elements representing the electrode assembly. The central core (cell center pin) was not separately

included in this model. Here, a more realistic cell model was developed with representation of the central core as a thin metal tube. Two types of punch loading were studied, deformation by a rigid rod, and indentation by a hemispherical punch, see Figure 3 Row a. The first type, which is the rigid rod indentation, was used to calibrate the tensile fracture strain, which was found to be $\epsilon_f=0.45$.

The local deformation and the cracking of the electrode assembly for both cylindrical cell models in the two loading cases are presented in matrix form in Figure 3. This is a complex figure in which the two columns show the two types of loading, and the rows give information on two types of models, output curves, and CT scan 3D rendering. For the original model (no central rod), it is seen (from Figure 6 Row b) that a transverse crack is predicted under both loading scenarios (rigid rod and spherical punch), which is consistent with the crack seen in the CT scan 3D renderings (Figure 6 Row d). The model predicts the load-displacement and location of short circuit very closely in both loading scenarios, Figure 3 Row c. In the case of the hemispherical punch load, small longitudinal cracks were also formed inside the electrode assembly, which was not apparent in the CT scan.

The second model (with representation of central core) also captured the formation of a cross sectional crack under the cylindrical rod indentation (Figure 3 Row e). The corresponding plot of load displacement shows a good correlation between the test and simulations through the loading process and at the peak value (see Figure 3 Row c). The prediction of transverse crack in the above simulations compares well with CT scan images of the actual cell. However, this model (with central core), was not as successful in simulating the hemispherical punch indentation (Figure 3 Row e, right). It showed a premature failure at much lower peak load and smaller displacement (see Figure 3 row c, right). The crack in the second model is developed in the longitudinal direction, while in the CT scan, crack is seen in the cross sectional (transverse) direction. It seems that the addition of a core in the model creates circumferential stresses, which were not present in the lumped model. In the real cell, sliding of the layers over each other can alleviate such stresses without failure. Lack of incorporation of anisotropy in the numerical material model leads to failure when a circumferential load is created (in the presence of a core), and creates a premature longitudinal crack. This is a clear deficiency of the simplified isotropic material model of the electrode assembly and shows a need for adding anisotropic properties to the material model.

Micro Testing- Uniaxial and Biaxial Tests of Electrode/Separators

In previous publications of the research team, the battery model had primarily involved calibration under compression loading. More precise behaviour prediction can be obtained if the models are refined by inputting details of tensile behaviour

of the multi-layer and multi-material system. The components of the electrode/separator assembly have thicknesses between 0.009 and 0.200 millimetres, which means performing tests on them would not be a trivial exercise due to their delicate nature. Cutting specimens, mounting them in the fixture of the loading frame, and producing repeatable results poses a real challenge. Although a few publications have reported on tensile testing of battery components^{15,16}, there is no standard test method available to follow. This section describes results of preliminary tensile tests on individual components and assembly of a multi-layer sample. Generic negative electrode (anode), positive electrode (cathode), current collector, and separator materials were purchased in non-assembled dry state from MTI Corporation. The cathode was LiCoO₂ coated on aluminium foil, and had a total thickness of 0.2 mm. The aluminium foil was 15 μm thick. The anode was CMS Graphite coated on 9 μm copper foil and had a total thickness of 0.1 mm. The polyethylene separator had a thickness of 16-25 μm . Overall, about fifty tests were performed on current collectors, anodes, cathodes, and separators in machine and transverse directions. All specimens were cut using a template and a sharp razor knife. The gage section of specimens was 5 mm wide and 10 mm long. At least five repeats were done for each test.

The tests were performed by an Instron Single Column TableTop load frame of 5940 series. The specimens were mounted on Instron soft grips, which provided sufficient strength without any slippage. Extra care was taken to avoid any eccentricity in the plane of the specimen and the grip alignment. The tests were performed with a constant prescribed crosshead velocity of 0.2 mm per minute. Fracture of foils was rather abrupt, while, the separator goes under very large strains before failure.

Measured load displacement curves for aluminium and copper foils in rolling direction and 90° to rolling direction are shown in Figure 4 a. It should be noted that not only was the force level of the aluminium foil smaller than that of the copper, it also fractured at a much lower displacement. Anisotropy was observed for the aluminium foil but not for the copper. The fracture of both foils happens on the hardening part of the curve before necking. Tests were also performed on complete anode and cathodes, consisting of foils coated by active electrode material. Because of the anisotropy observed in the aluminium foil, tests on cathode were performed both in rolling and 90° to rolling directions. Anode specimens were tested only in MD because no anisotropy was observed for the bare copper foil. One important observation here was that added thicknesses of coating particles on the anode and cathode not only did not increase the force, in fact they significantly reduced the load levels and displacement to fracture when compared to bare foils without coating. It is believed that the reason for this reduced strength should be the calendaring process, which causes intrusion of particles into the metal foil and creates weak points for the foil, see Figure 4c. The foils might also have been etched before calendaring and that could have reduced their strength too.

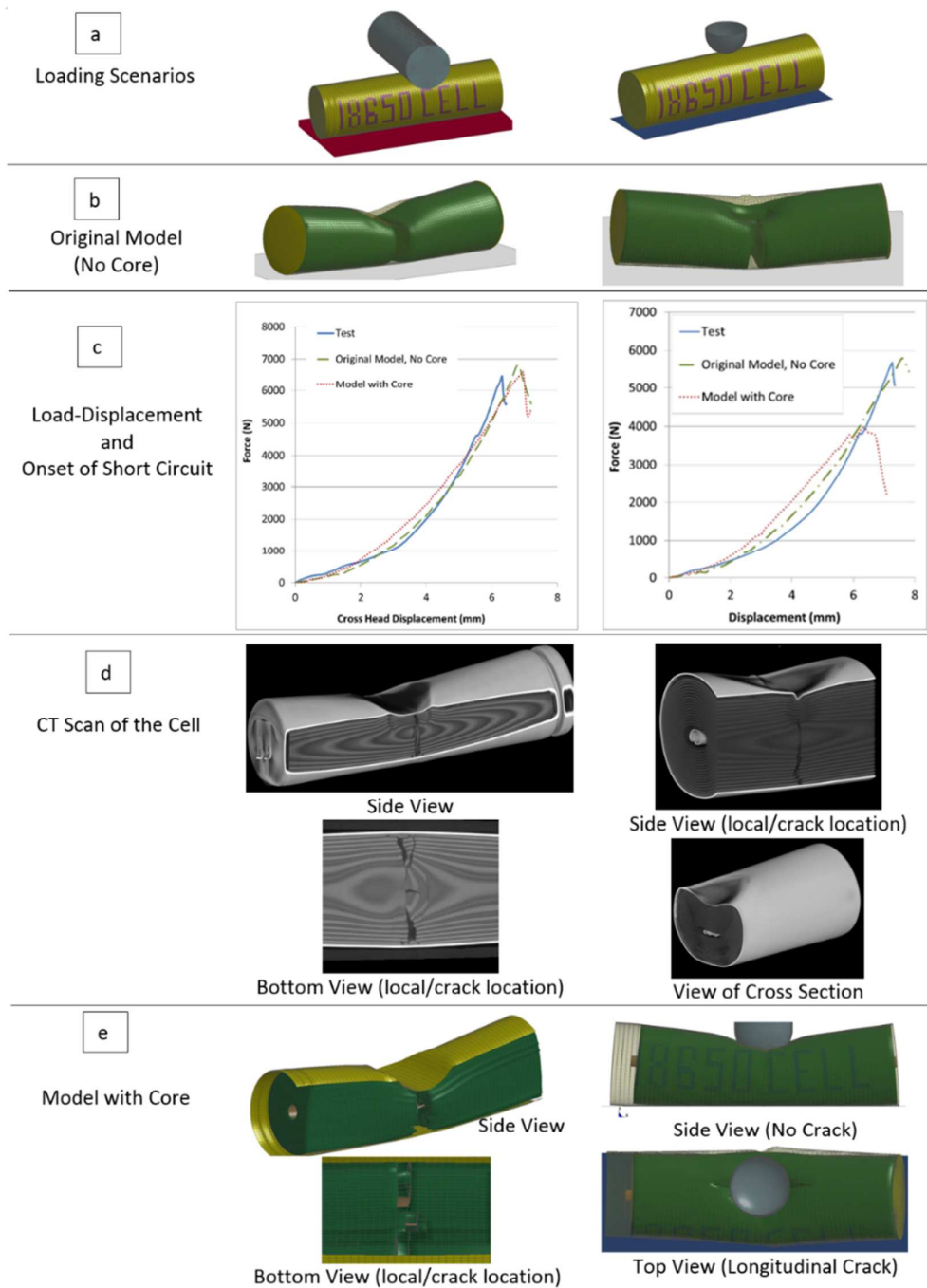


Figure 3: Simulation of the crack through element erosion using the two models for 18650 cell

Stress-strain curves for bare aluminium and copper foils as well as coated anodes and cathodes are included in Appendix 2. Several observations can be made based on the above tests. First, the strength of the anode is almost twice the strength of the cathode (24 MPa versus 12 MPa). Second, the fracture strain of the anode is an order of magnitude larger than that of

the cathode (0.06 versus 0.006). The above features make development of a failure model for the jelly roll a challenging task.

The results of the tests on the separator in Machine and Transverse Directions (MD and TD) are shown in Figure 4b, in perspective with Force-displacement response of other layers reported from Figure 4a. There is an extremely strong

anisotropy in the separator, which is one of the important properties that must be included in more advanced models of the electrode assembly. A Scanning Electron Microscope (SEM) photo of the separator (Figure 4c) illustrates the pores and fibres produced due to crazing process during manufacture of these separators and the cause of the anisotropic structure.

In the next step, tests were performed on an assembly of one cathode, one anode, and two layers of separator. This is the basic building block of a lithium-ion battery electrode assembly, which repeats itself from layer to layer. The blue solid line in Figure 4e) represents the load displacement curve measured in the machine direction. The purple dashed line was created by superimposing the loads measured from individual components. The two curves are close to one another providing a verification of the correctness of the measuring technique of individual thin layers. More uniaxial and biaxial tests of battery components in a dry versus soaked state are under preparation.

Anisotropic Material Model for the electrode assembly and Calibration

To incorporate the anisotropic properties of the jelly roll in the model, Material 126 of the LS Dyna library has been chosen. The set of equations describing this material involves two concepts:

The hardening curve,

$$Y_{ij} = Y_{ij}^0 + H_{ij}(\epsilon_{ij}) \quad (4)$$

where Y_{ij} is the yield stress, and Y_{ij}^0 is the initial yield limit, and ϵ_{ij} is the engineering strain.

The failure criterion is:

$$\text{Max}(\epsilon_{ii}) = \text{Constant} \quad (\text{no summation}) \quad (5)$$

where ϵ_{ii} are the normal strains in tension.

Considering our test data, the range of elastic response is negligible. Therefore, it is assumed that initial yield shrinks to a point, $Y_{ij}^0=0$. By contrast to the isotropic hardening, the model is fully defined by prescribing six hardening curves (three

normal and three shear) in MD, TD, and through-thickness directions. In addition, the normal components of stresses are different in tension and compression. At the same time, shear response of the material is assumed to be symmetric when changing load direction. It is further assumed that the shear strength is equal to $\frac{1}{2}$ of the compression strength.

Calibration: For the complete calibration, three compression and three tension curves in three directions are needed. It is assumed that the compressive properties are similar in the MD and TD directions, and only different in the through-thickness direction. Compression properties of the studied cells were determined in a previous publication of the present authors³, (see Figure 5a). The tests were done in the state of uniaxial strain/stress because the Poisson's ratio was almost zero.

It should be noted that the compressive curves here are result of aggregate response of all the layers of the electrode assembly (electrode/separator/electrolyte). Similarly, average properties must also be determined in tension for the representative volume element of the cell. The tensile tests explained above were done on generic materials purchased from MTI Corporation and they did not have same thicknesses as the layers of the actual cells, as measured in³. Therefore, we cannot use the curve from Figure 4e directly, and it is proposed to define a weighted average for a system of layers undergoing same strain,

$$\sigma_{average} = \frac{\sum \sigma_l t_l}{\sum t_l} \quad (6)$$

where

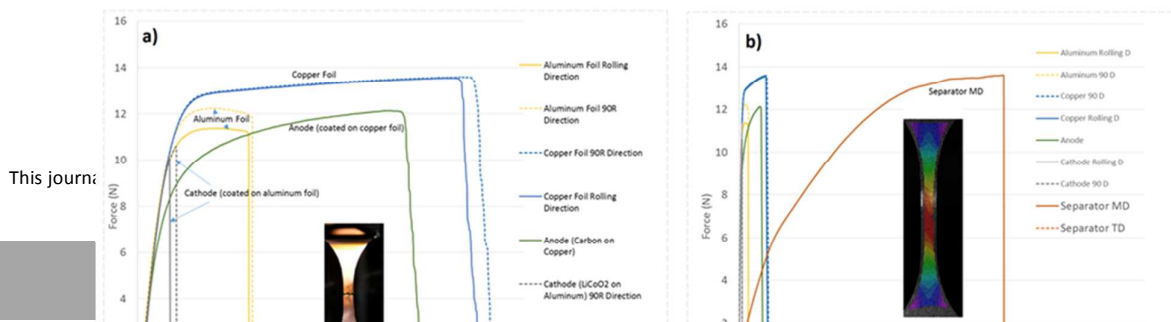
$$\sigma_l = [\sigma_{Al\ foil}, \sigma_{Cu\ foil}, \sigma_{active\ coating}, \sigma_{separator}]$$

$$t_l = [t_{Al\ foil}, t_{Cu\ foil}, t_{active\ coating}, t_{separator}]$$

RSC ADVANCES

ARTICLE

Figure 4: a) Force-displacement response of specimens cut from anode, cathode, and bare aluminium and copper foils, under uniaxial tensile loading; b) Force-displacement response of separator in MD and TD; c) Intrusion of cathode particles into aluminium foil as seen in Scanning Electron Microscope (SEM) image of a Li-ion cell cross-section (courtesy of Exponent); d) Anisotropic structure of a separator as seen in an SEM image e) Comparison of the multi-layer test load-displacement result with load-displacement curve estimated by summing contribution of each layer



This journal

0, 1-3 | 7

ARTICLE

Journal Name

RSC Advances Accepted Manuscript

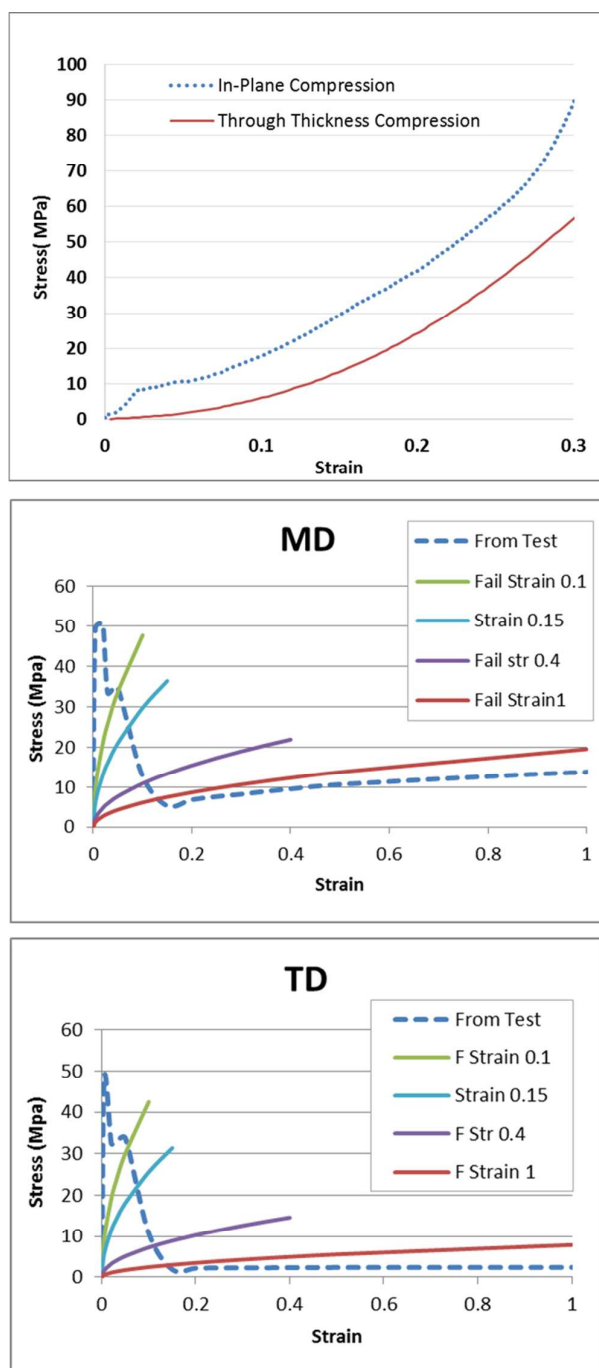


Figure 5: a) Compressive stress – strain curves, measured in in-plane and out of plane directions³, b) The average curve for an RVE consisting of all layers in tension, and the smooth hardening curves calculated with different fracture strains

The averaging should be performed separately in Machine and Transverse directions. In the through- thickness direction, because of delamination, tensile properties cannot be measured.

The tensile strength of the active coating comes primarily from the strength of the binder. This justifies an assumption that properties of the anode and cathode coatings are similar in tension. These properties were taken from Liu et al 2009¹⁷.

The total thickness of the assembly is $t_{total} = \sum t_i = 0.24 \text{ mm}$.

As it can be seen from Figures 4e and 5b, there are sequential hardening and softening phases in the averaged stress-strain curve. In the numerical simulation, the presence of material softening creates an unstable response. To circumvent this difficulty, the tensile properties have been smoothed over the range of expected strains by calculating the energy absorbed during the loading process, up to the fracture strain. This energy is assumed to be equal to the energy of an equivalent power law constitutive property:

$$E = \int_0^{\epsilon_f} \sigma_{average}(\epsilon) d\epsilon = \int_0^{\epsilon_f} A \epsilon^n d\epsilon \quad (7)$$

The failure strain causing short circuit is controlled by the failure of the separator. From Figure 4b, it can be inferred that the stress-strain curve of the separator in MD direction can be well fitted by a power law with an exponent of $n=0.5$. In the TD direction, it can be seen that the element has gone through necking very early during deformation. Therefore, it is hard to detect the failure strain from the tests, and trial finite element simulations should be performed to estimate the failure strain for the separator. Considering the multi stage failure of the RVE, depending on the point of failure for the separator, the average smooth curve representing the average properties of all layers would be very different. For the trial simulations, for each value of chosen fracture strain, the amplitude of the power law, A , can be calculated from the above equation. The smooth representative curves have higher strengths if a small value is chosen for the failure strain, because at those strains the contribution of foil is the dominant factor. The smooth curves in MD and TD are not too different for small failure strain cases. As the chosen failure strain increases, the contribution of the foil fades and the curves have lower values, thus the dominance of separator behaviour is observed. With the dominance of separator properties, those curves are more anisotropic as well.

Trial simulations were performed by taking the equivalent smooth curves as input for tensile properties in MD and TD directions. In the out of plane (through-thickness) direction, the layers cannot take any tensile stress, as delamination will occur in reality. This property could not be incorporated into the current material model, because the failure strain is considered similar in the three directions; therefore, a small through-thickness tension would lead to an unrealistic failure of the elements. For that reason, it is assumed that tensile strength in the through-thickness direction is equal to that in the TD direction. Such a model will predict the failure correctly, but will not represent delamination of layers.

Results of Anisotropic Model Application for Small Pouch and 18650 Cylindrical Cells

Small Pouch Cell

In this section, it will be shown what types of improvements are achieved by replacing the isotropic constitutive model of the cell with the new anisotropic model, calibrated in previous section. Figure 6 shows the crack orientations for the small pouch cell under hemispherical loading, assuming three trial failure strains for the RVE. It was observed that at small failure strains of 0.1 and 0.15, the crack is developed in both transverse and machine directions resembling the shape of a cross. At these small strains, foil failure plays a more important role and the fracture develops in a similar way in two directions as the foils are relatively isotropic. At larger fracture strains of 0.4 and 1.0, cracks develop parallel to the transverse direction of the separator, while less extensive damage is seen in the machine direction. These cracks are more aligned with those observed in the CT scan of the cell. From comparison of load-displacement in the three simulations, it is inferred that the correct value of fracture strain is closer to 0.4, as the simulation with this value provides the closest estimate for the onset of short circuit. From the above results it is interesting to note that information on the crack orientation from the CT scan is an important factor in correctly calibrating the material and failure model. A clear benefit of working with the anisotropic model of the jelly roll is that in contrast with the isotropic model (seen Figure 2), it provides a better prediction of the crack initiation.

Cylindrical Cell

No additional tests or measurements were available for the jelly roll of the cylindrical cell. Therefore, the smooth tensile curve calculated for a failure strain of 0.4 for the pouch cell was scaled by a factor of 10/25 to estimate the tensile

properties for the cylindrical cell model. This scale factor was

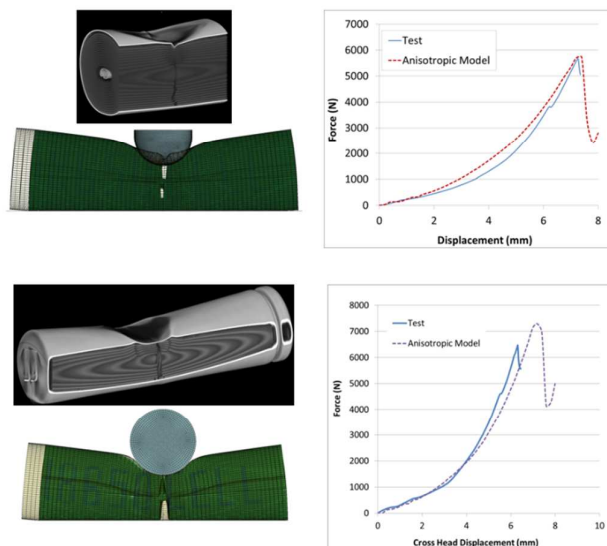


Figure 6: Development of crack in cross section of the cell, when using the anisotropic material model

chosen based on proportion of tensile cut-off values of the two cells as reported by Sahraei et al 2014⁴. Figure 7 shows the simulation of a cylindrical cell with the anisotropic material model and the load-displacement output. As it can be seen, a crack is now developed in the cross section of the cell under the punch in both loading scenarios. This cross sectional crack is consistent with the CT scan of the cell. Therefore, the anisotropic pouch model is one step closer to the real test than the isotropic model. There was also a major improvement in the predicted load displacement under hemispherical punch

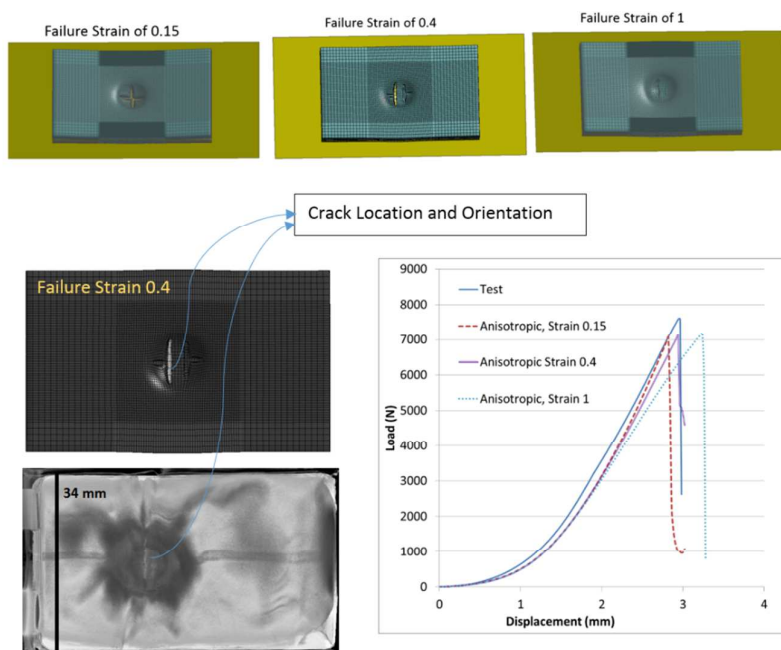


Figure 7 : Location of crack and comparison of load-displacement curves. Simulations were performed with anisotropic pouch cell model at assumed failure strains of 0.15, 0.4, and 1

loading, with peak load of about 6,000 N, when compared with the isotropic model (with central core), which showed a premature failure at a load of about 4,000 N. However, the limitation of this model is that besides the cross sectional crack that was expected from CT scanning, still a longitudinal crack is developed under the hemispherical punch simulation, which was not seen in the CT scan. An anisotropic failure model is under development to overcome this limitation.

Discussion and Conclusion

Two types of material models for electrode assemblies, isotropic and anisotropic, were used to simulate local deformation and damage of batteries. The previously developed isotropic model had been calibrated for small pouch and 18650 cylindrical cells in ^{1,3,4}. New experiments were reported here to calibrate the new anisotropic model for both small pouch and cylindrical cells. The isotropic lumped modes of both cylindrical and pouch cells closely predicted the load-displacement and point of short circuit. The isotropic model also correctly predicted the crack location for a model of an 18650 cell when the electrode assembly and central core (and hole) were modelled lumped together with one type of solid element. However, the isotropic model of the pouch cell predicted a cylindrical failure area under the punch which did not match the CT scan for the actual cell, which revealed a linear crack perpendicular to the transverse direction of the cell. Also, when a detailed model of 18650 cell was created with the central core modelled separately, the model showed a premature crack under spherical loading. To improve the model, a set of experiments were performed including the tensile properties of the individual components of the electrode assembly (electrode active materials, separators, and current collectors). These tests revealed the anisotropic nature of the material response. Therefore, a similar model was developed, calibrated using the test data, and used to simulate the loading scenarios were the isotropic model was not able to predict location of failure properly. This new model provided improved capability in predicting correct crack orientation.

To put this discussion in a different context, it should be pointed out that there are advantages and disadvantages of both models presented in this paper. The isotropic model is simpler and requires fewer tests for calibration, yet it gives reasonable results for most loading cases. At the same time, an anisotropic model improves the results for cases where unsatisfactory results were obtained with the isotropic model. Note that the anisotropic model is more complex and involves new material parameters that should be calibrated from additional testing.

Despite the noticeable improvements in the present anisotropic model, it is still not perfect in predicting the exact size of the cracked region and sometimes there are small cracks in locations that were not expected based on CT scanning of the cells. One reason could be that the model was calibrated from dry, generic materials and not the actual wetted components inside the electrode assemblies of the

cells. Another shortcoming of the current model is that although the flow model is anisotropic, the failure model is still the same in all directions. In actual lithium-ion cells, tensile strains through the thickness would result in delamination of the layers and would not necessarily lead to short circuiting. This feature should be included in the failure model of the cell, where large strains in this direction would be treated differently and would not cause element failure.

The methods developed in this research could be easily applied to pouch and cylindrical batteries with different chemical compositions or geometric lay up of layers. The isotropic version of the model had been applied to different pouch cells and yielded precise results ⁴. However, the calibration should be followed and repeated to calculate the needed parameters for the specific desired cell. X-ray of the cells presented in Sahraei et al 2014 ⁴ and validation of anisotropic model for those cells was not possible in this study due to size limitation of the CT-Scan machine. Having different coating methodologies, type of material or additive will change the values of calibration parameters however is not expected to affect validity of the method itself.

It should be noted that the purpose of this study was to detect onset and location of short circuit in the cell due to mechanical abuse. For this purpose the model was capable to predict deformation, force, and geometry of the cell through loading and up to onset of short circuit. The low SOC status of cells prevented them from going to thermal runaway and therefore location of crack and failure could be investigated using X-ray. Had the cells been fully charged, they would have more thermal reactions after short circuit and that could change the shape of failure surface and make the investigation extremely difficult. At the same time, it should be noted previous investigations have shown that SOC does not change mechanical response of cell before short circuit ¹⁸, which means it is expected that cells would behave similarly before short circuit and have similar type of mechanical failure at onset of short circuit even if they had been charged. The only thing that is expected to be different for a charged cell is chemical reactions after failure. There are several models on predicting chemical/thermal reactions in the cell after short circuit. That topic was not subject of current study, but such models could be coupled with the current model to predict reaction of the cell after short circuit.

Acknowledgements

The authors would like to thank LT Kyle Miller for providing the SEM image of the separator. We also like to acknowledge support of Ford-MIT Alliance, National Energy Renewable Lab, and MIT Battery Modelling Consortium for this research. Support of Altair Company with HyperWorks software is also greatly appreciated.

References

- 1 E. Sahraei, J. Campbell and T. Wierzbicki, *J. Power Sources*, 2012, **220**, 360–372.
- 2 Y. Xia, T. Wierzbicki, E. Sahraei and X. Zhang, *J. Power Sources*, 2014, **267**, 78–97.
- 3 E. Sahraei, R. Hill and T. Wierzbicki, *J. Power Sources*, 2012, **201**, 307–321.
- 4 E. Sahraei, J. Meier and T. Wierzbicki, *J. Power Sources*, 2014, **247**, 503–516.
- 5 T. Wierzbicki and E. Sahraei, *J. Power Sources*, 2013, **241**, 467–476.
- 6 L. Greve and C. Fehrenbach, *J. Power Sources*, 2012, **214**, 377–385.
- 7 W.-J. Lai, M. Y. Ali and J. Pan, *J. Power Sources*, 2014, **245**, 609–623.
- 8 M. Y. Ali, W.-J. Lai and J. Pan, *J. Power Sources*, 2013, **242**, 325–340.
- 9 Z. J. Zhang, P. Ramadass and B. Fang, in *29th international Battery Seminar and Exhibit*, 2012, vol. 1, p. 62276.
- 10 G.-H. Kim, A. Pesaran and R. Spotnitz, *J. Power Sources*, 2007, **170**, 476–489.
- 11 A. a. Pesaran, *J. Power Sources*, 2002, **110**, 377–382.
- 12 R. M. Spotnitz, J. Weaver, G. Yeduvaka, D. H. Doughty and E. P. Roth, *J. Power Sources*, 2007, **163**, 1080–1086.
- 13 V. Yufit, P. Shearing, R. W. Hamilton, P. D. Lee, M. Wu and N. P. Brandon, *Electrochem. commun.*, 2011, **13**, 608–610.
- 14 I. Manke, J. Banhart, a. Haibel, a. Rack, S. Zabler, N. Kardjilov, a. Hilger, a. Melzer and H. Riesemeier, *Appl. Phys. Lett.*, 2007, **90**, 214102.
- 15 K. H. Shim, S. K. Lee, B. S. Kang and S. M. Hwang, *J. Mater. Process. Technol.*, 2004, **155-156**, 1935–1942.
- 16 A. Sheidaei, X. Xiao, X. Huang and J. Hitt, *J. Power Sources*, 2011, **196**, 8728–8734.
- 17 P. Liu, E. Sherman and A. Jacobsen, *J. Power Sources*, 2009, **189**, 646–650.
- 18 J. D. Meier, E. Sahraei, M. Salk, T. Kisters and F. Huberth, in *Battery Congress*, 2013.

The system features a Kevex KM13106E 130 kV X-ray tube equipped with a collimator. The X-ray tube was operated at 130 kV and 120 μ A, corresponding to a spot size of 20 μ m. The image intensifier is a 2D panel with 1024x144 elements; both the X-ray tube and the image intensifier are stationary while the samples rotate on a turntable part manipulator. Distortion correction and computed tomography processing of the raw radiographs were performed using the BIR ACTIS 5 software package.

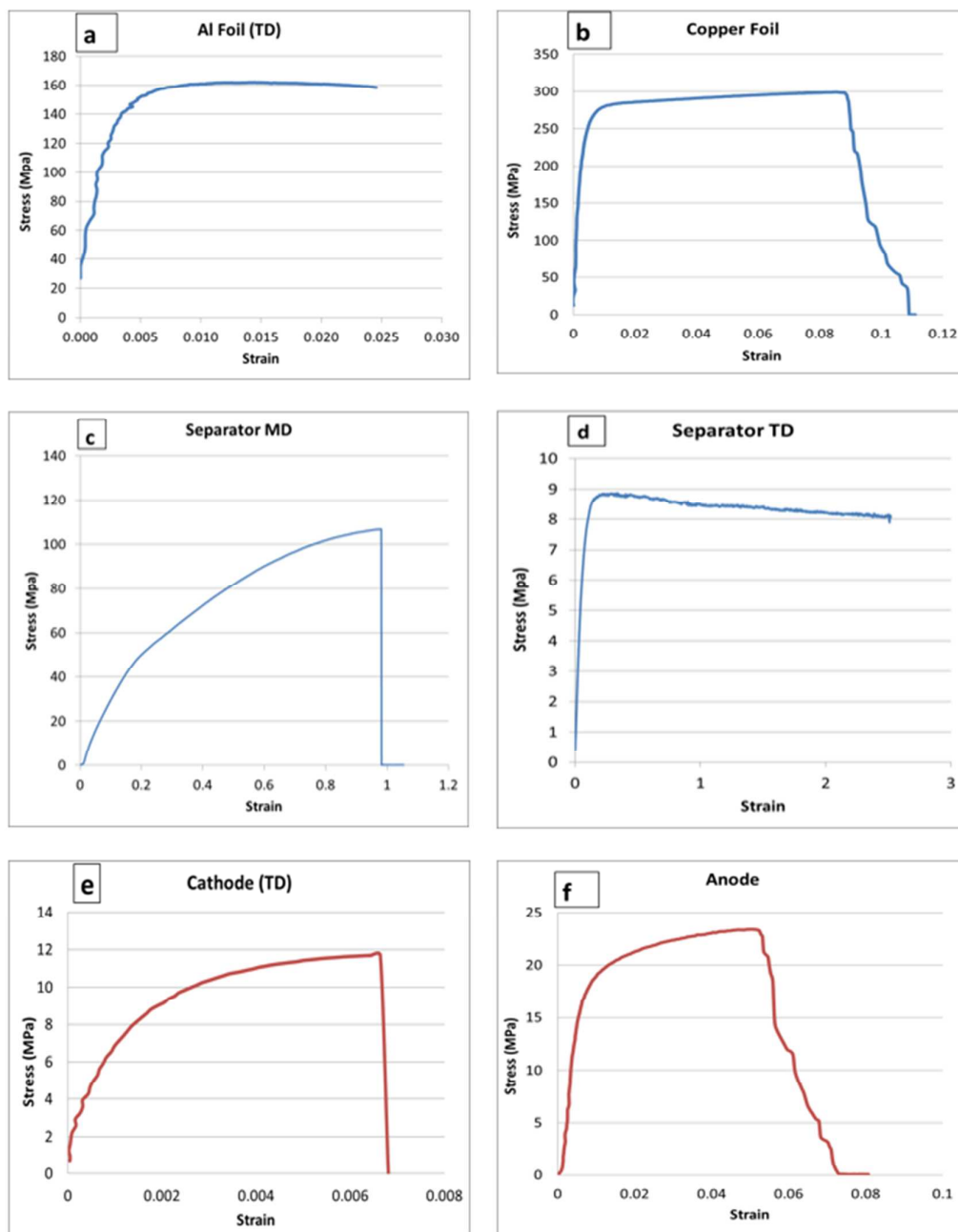
Sample preparation was accomplished by affixing them to radiography-neutral plastic fixtures with modelling clay. Each sample was affixed such that the longer axis of the object was parallel to the axis of rotation. For convention, we considered the axis of rotation the Z-axis and the perpendicular the X-Y plane. Each sample was positioned such that its radiograph, taken at its widest point, fills approximately 80-90% of the image intensifier width. Since the image intensifier has 1024 elements of width, the in-plane (X-Y plane) resolution of an object is approximately given by: (widest dimension of the object) / (percentage of image intensifier utilized) / 1024. For a new 18650 cell, that is approximately 18 mm in diameter, the typical in-plane resolution in this configuration would be approximately 22 μ m. The sample fixture and samples were then rotated through the X-ray beam by the part manipulator, and a series of radiographs were collected by the ACTIS 5 software at each angle of rotation. This process was repeated at all necessary Z-height positions until each location throughout the height of the sample had been scanned.

In total, each battery sample was imaged using 3000 views per full rotation and 10 averages per view. The ACTIS 5 software then processed the thousands of raw radiographs to reconstruct a series of two-dimensional "slices." A slice is a virtual cross-section of an object in an X-Y plane that represents a portion of the object's overall Z height; it is perpendicular to the axis of rotation. Each slice in the resulting data set is a greyscale 16-bit TIFF image file.

In the case of the 18650 cell, the slice thickness was 30 μ m, for a total of 2215 slices, and the resulting X-Y pixel dimensions were 22.46 μ m. For the soft pouch cell, the slice thickness was 50 μ m, for a total of 1181 slices, and the resulting X-Y pixel dimensions were 32.71 μ m. Since each slice contains X and Y dimensional information about the sample and represents a certain Z thickness, the slices can be combined to construct a 3D volume. The 3D volume can be rendered using computer graphics and manipulated to create virtual cross-sections through arbitrary planes in any orientation.

Appendix 1- Details of CT Scanning Technique

Appendix 2-Stress-Strain Curves for Battery Components



Appendix Figure 1: Stress-Strain Curves in Uniaxial loading of a)Aluminium foil, b)Copper foil, c)Separator MD, d)Separator TD, e)Cathode MD and TD, and f)Anode